

EUROPEAN ORGANISATION FOR NUCLEAR RESEARCH (CERN)



Submitted to: Physics Letters B

CERN-EP-2022-135
24th May 2025

Measurement of the Higgs boson mass in the $H \rightarrow ZZ^* \rightarrow 4\ell$ decay channel using 139 fb^{-1} of $\sqrt{s} = 13 \text{ TeV}$ $p p$ collisions recorded by the ATLAS detector at the LHC

The ATLAS Collaboration

The mass of the Higgs boson is measured in the $H \rightarrow ZZ^* \rightarrow 4\ell$ decay channel. The analysis uses proton–proton collision data from the Large Hadron Collider at a centre-of-mass energy of 13 TeV recorded by the ATLAS detector between 2015 and 2018, corresponding to an integrated luminosity of 139 fb^{-1} . The measured value of the Higgs boson mass is $124.99 \pm 0.18(\text{stat.}) \pm 0.04(\text{syst.}) \text{ GeV}$ and is based on improved momentum-scale calibration for muons relative to previous publications. The measurement also employs an analytic model that takes into account the invariant-mass resolution of the four-lepton system on a per-event basis and the output of a deep neural network discriminating signal from background events. This measurement is combined with the corresponding measurement using 7 and 8 TeV $p p$ collision data, resulting in a Higgs boson mass measurement of $124.94 \pm 0.17(\text{stat.}) \pm 0.03(\text{syst.}) \text{ GeV}$.

Contents

1	Introduction	2
2	ATLAS detector	3
3	Data and event simulation	4
4	Muon and electron reconstruction	5
5	Event selection	7
5.1	Signal–background discriminant	8
5.2	Event-level $m_{4\ell}$ resolution	8
6	Signal and background model	12
7	Results	14
8	Summary	18

1 Introduction

The observation of a Higgs boson, H , in 2012 by the ATLAS and CMS collaborations [1, 2] in proton–proton (pp) collisions produced by the Large Hadron Collider (LHC) was a major step towards understanding the mechanism of the electroweak (EW) symmetry breaking [3–5]. An unknown parameter of the Standard Model (SM), the Higgs boson mass m_H , is related to the SM vacuum stability [6] and its value is required for precise calculations of electroweak observables, including the production and decay properties of the Higgs boson itself. These calculations are needed to test the coupling structure of the SM Higgs boson, as suggested in Ref. [7] and references therein. Therefore, it is important to determine the Higgs boson mass experimentally.

The mass of the Higgs boson was measured to be 125.09 ± 0.24 GeV [8] in a combined analysis performed by the ATLAS and CMS collaborations using approximately 25 fb^{-1} of $\sqrt{s} = 7$ and 8 TeV pp collision data recorded in 2011 and 2012, respectively, commonly referred to as Run 1. The individual measurements, reported in Refs. [9, 10], used the $H \rightarrow ZZ^* \rightarrow 4\ell$ (where $\ell = e$ or μ) and $H \rightarrow \gamma\gamma$ decay modes because of their excellent mass resolution.

The ATLAS Collaboration reported a measurement of m_H using the $H \rightarrow ZZ^* \rightarrow 4\ell$ and $H \rightarrow \gamma\gamma$ channels with 36.1 fb^{-1} of $\sqrt{s} = 13$ TeV pp collision data recorded in 2015 and 2016. This was combined with the Run 1 ATLAS measurement to obtain a value of $m_H = 124.97 \pm 0.24$ GeV [11]. The CMS Collaboration measured m_H using the $H \rightarrow ZZ^* \rightarrow 4\ell$ and $H \rightarrow \gamma\gamma$ channels with 35.9 fb^{-1} of $\sqrt{s} = 13$ TeV pp collision data recorded in 2015 and 2016. This was combined with the Run 1 CMS measurement to obtain a value of $m_H = 125.38 \pm 0.14$ GeV [12].

This paper reports a new measurement of m_H in the $H \rightarrow ZZ^* \rightarrow 4\ell$ channel using a 139 fb^{-1} dataset of 13 TeV pp collisions produced by the LHC and recorded by the ATLAS detector between 2015 and 2018, commonly referred to as Run 2. Most of the techniques used in this analysis are described in detail in Ref. [13].

The $H \rightarrow ZZ^* \rightarrow 4\ell$ process is identified by selecting four leptons in the final state, and requiring two of them to be compatible with originating from a Z -boson decay. The mass measurement is performed using an analytic model to describe the distribution of the reconstructed 4ℓ invariant mass, $m_{4\ell}$, as a function of m_H and to fit to the observed distribution. In comparison with the previous ATLAS result from the $H \rightarrow ZZ^* \rightarrow 4\ell$ channel [11], the measurement has been improved by using the complete Run 2 dataset and a new high-precision muon momentum calibration. The m_H uncertainty has also been reduced by introducing a neural-network-based classifier to discriminate between signal and background processes and by including the event-by-event invariant-mass resolution of the four-lepton system in the analytic model used to fit the collision data.

This paper is organised as follows. The ATLAS detector is described in Section 2, and the data samples and Monte Carlo simulations are presented in Section 3. The reconstruction of muons and electrons, as well as their calibration procedures, is discussed in Section 4, while the event selection is explained in Section 5. The statistical models describing the signal and background samples are defined in Section 6 and results of the measurement are presented in Section 7. The conclusions are provided in Section 8.

2 ATLAS detector

The ATLAS experiment [14] at the LHC is a multi-purpose particle detector with nearly 4π coverage in solid angle.¹ It includes an inner tracking detector (ID) used for charged-particle tracking, surrounded by a 2 T solenoid. Electromagnetic (EM) and hadronic calorimeters are placed outside the solenoid, followed by a muon spectrometer (MS).

The ID provides precise reconstruction of tracks within a pseudorapidity range $|\eta| \leq 2.5$. The high-granularity silicon pixel detector covers the vertex region and typically provides four measurements per track, the first hit normally being in the insertable B-layer (IBL) installed before Run 2 [15, 16]. It is followed by the silicon microstrip tracker, which usually provides eight measurements per track. These silicon detectors are complemented by the transition radiation tracker (TRT), which enables radially extended track reconstruction up to $|\eta| = 2.0$. The TRT also provides electron-identification information based on the detection of transition radiation X-ray photons.

The ATLAS calorimeter system covers the pseudorapidity range $|\eta| < 4.9$, with finer granularity over the region matching the inner detector. The lead/liquid-argon (LAr) EM calorimeter is divided into two half-barrels ($|\eta| < 1.475$) and two endcap components ($1.375 < |\eta| < 3.2$). It is segmented into three longitudinal (depth) sections over the region $|\eta| < 2.5$, and into two depth sections for $2.5 < |\eta| < 3.2$. Hadronic calorimetry is provided by the steel/scintillator-tile calorimeter, segmented into three barrel structures within $|\eta| < 1.7$, and two copper/LAr hadronic endcap calorimeters extending the coverage to $|\eta| = 3.2$. The solid angle coverage is completed with forward copper/LAr and tungsten/LAr calorimeter modules optimised for electromagnetic and hadronic energy measurements, respectively.

The muon spectrometer, located beyond the calorimeters, is designed to detect muons in the region $|\eta| < 2.7$ and to provide momentum measurements with a relative resolution better than 3% over a wide range of

¹ ATLAS uses a right-handed coordinate system with its origin at the nominal interaction point (IP) in the centre of the detector and the z -axis along the beam pipe. The x -axis points from the IP to the centre of the LHC ring, and the y -axis points upwards. Cylindrical coordinates (r, ϕ) are used in the transverse plane, ϕ being the azimuthal angle around the z -axis. The pseudorapidity is defined in terms of the polar angle θ as $\eta = -\ln \tan(\theta/2)$. Angular distance is measured in units of $\Delta R \equiv \sqrt{(\Delta\eta)^2 + (\Delta\phi)^2}$.

transverse momentum, p_T , and up to 10% at $p_T \sim 1$ TeV. A system of three superconducting air-core toroidal magnets provides a magnetic field with a bending power of approximately 2.5 Tm in the barrel and up to 6 Tm in the endcaps.

A two-level trigger system [17] is used to select events. The first-level trigger is implemented in hardware and uses a subset of the detector information to accept events at a maximum rate of about 100 kHz. This is followed by a software-based trigger that reduces the accepted event rate to 1 kHz on average. An extensive software suite [18] is used in the reconstruction and analysis of real and simulated data, in detector operations, and in the trigger and data acquisition systems of the experiment.

3 Data and event simulation

This measurement uses data from pp collisions with a centre-of-mass energy of 13 TeV collected between 2015 and 2018 using single-lepton, dilepton, and trilepton triggers [19, 20] as detailed in Ref. [13]. The combined efficiency of these triggers is approximately 98%, 99%, 97%, and 99% for the 4μ , $2\mu 2e$, $2e 2\mu$, and $4e$ final states, respectively, for the simulated $H \rightarrow ZZ^* \rightarrow 4\ell$ events passing the event selection described in Section 5 (assuming $m_H = 125$ GeV). After data-quality requirements are imposed, the integrated luminosity of the data sample is 139 fb^{-1} [21].

Details of the simulated Monte Carlo (MC) events used in this analysis can be found in Refs. [13, 22]. Higgs boson production via the gluon–gluon fusion (ggF) process was modelled at next-to-leading-order (NLO) accuracy in the strong coupling constant α_s using the PowHEG NNLOPS generator [23–31] with the PDF4LHC15NNLO set of parton distribution functions (PDFs) [32]. Higgs bosons produced via vector-boson fusion (VBF), in association with a vector boson (VH) or in association with a top-quark pair ($t\bar{t}H$), were simulated at NLO accuracy with the PowHEG Box generator [25–27], using the PDF4LHC15NLO PDF set. The $gg \rightarrow ZH$ process was also simulated with the PowHEG Box generator, but at leading-order (LO) accuracy. Higgs boson production in association with a top quark (tH) or with a bottom-quark pair ($b\bar{b}H$) was simulated at NLO accuracy using the MADGRAPH5_AMC@NLO generator [33, 34] with the NNPDF3.0 PDF set [35]. For all signal processes, the EvtGEN 1.2.0 generator [36] was used for the simulation of the bottom- and charm-hadron decays. Correspondingly, the PYTHIA 8 generator [37] was used for the $H \rightarrow ZZ^* \rightarrow 4\ell$ decay as well as for parton showering, hadronisation, and simulation of the underlying event. Higgs bosons produced via the ggF and VBF processes or in association with a vector boson were simulated for a range of m_H values from 123 to 127 GeV. Higgs boson production in association with a top quark, a top-quark pair, or a bottom-quark pair were simulated assuming $m_H = 125$ GeV. These samples are normalised to cross-sections obtained from the most recent predictions provided by the LHC Higgs Working Group [7].

The ZZ^* continuum background, separated into quark-initiated ($qqZZ$), gluon-initiated ($ggZZ$), and vector-boson scattering (EW ZZ) production, was modelled using the SHERPA 2.2.2 generator [38–41] with the NNPDF3.0NNLO PDF set. These samples are normalised to cross-sections obtained directly from the SHERPA simulation. Alternative $qqZZ$ samples, produced with the PowHEG Box v2 and MADGRAPH5_AMC@NLO generators, are used for studies of the systematic uncertainties. For the alternative samples, the PYTHIA 8 generator was used for parton showering, hadronisation, and simulation of the underlying event.

Backgrounds from WZ production and $t\bar{t}$ events were modelled using the PowHEG Box v2 generator, while Z bosons produced in association with jets were simulated using the SHERPA 2.2.1 generator. Minor contributions from processes with three electroweak bosons, denoted by VVV , were modelled using

SHERPA 2.2.2. Small backgrounds originating from top-quark production in association with one or more electroweak bosons or additional top quarks, such as $t\bar{t}Z$, $t\bar{t}WZ$, $t\bar{t}WW$, $t\bar{t}WZ$, $t\bar{t}Z\gamma$, $t\bar{t}ZZ$, ttt , $tttt$, and tZ (denoted by tXX), were simulated using the **MADGRAPH5_AMC@NLO** generator. The **PYTHIA 8** generator was used for parton showering, hadronisation, and simulation of the underlying event.

Generated events were processed through the ATLAS detector simulation [42] within the **GEANT4** framework [43] and reconstructed in the same way as collision data. Additional pp interactions in the same or neighbouring bunch crossings, referred to as pile-up, are included in the simulation. The pile-up events were modelled using the **PYTHIA 8** generator with the A3 set of tuned parameters [44] and the **NNPDF2.3LO** PDF set [45].

The normalisation of the non-resonant ZZ^* background component is determined by the fit of a signal and background model to the observed $m_{4\ell}$ distributions. The normalisations of the backgrounds from hadrons or hadron-decay products misidentified as prompt leptons, and from $Z+jets$, $t\bar{t}$ and WZ processes (referred to as the reducible background), are determined using data-driven techniques, and are explained in detail in Ref. [13].

4 Muon and electron reconstruction

Muon candidates are reconstructed using a combination of different algorithms [46]. The reconstruction of muon candidates within $|\eta| < 2.5$ is primarily performed by a global fit of reconstructed tracks in the ID and the MS. In the central detector region ($|\eta| < 0.1$), where the MS has reduced geometrical coverage, muons are also identified by matching a reconstructed ID track to either an MS track segment ('segment-tagged muons') or a calorimetric energy deposit consistent with a minimum-ionising particle ('calorimeter-tagged muons'). Calorimeter-tagged muons are required to have $p_T > 15$ GeV. For both the segment-tagged and calorimeter-tagged muons, the muon momentum is measured from the ID track alone. In the forward MS region ($2.5 < |\eta| < 2.7$) outside the ID coverage, MS tracks with hits in three MS layers are accepted as 'stand-alone muons' and combined with track segments formed from hits in the silicon tracker, if they exist. Additionally, 'loose' muon-identification criteria [46] are applied to reject low-quality tracks that have missing hits in the MS or have poor agreement between the reconstructed MS and ID tracks. Muons are required to be isolated by using both calorimeter-based and track-based isolation variables and applying the 'PflowLoose' criteria [46].

Although the detector is well aligned overall, there are residual local misalignments that bias the reconstructed muon-track sagitta [47, 48] and introduce a small, charge-dependent, momentum bias. The bias is measured with an iterative procedure that minimises the observed width of the line-shape of $Z \rightarrow \mu^+ \mu^-$ decays [49]. This correction, which is applied to the collision data, reduces the width of the dimuon invariant-mass distribution in Z -boson decays by approximately 1% [49]. A systematic uncertainty is assigned to this correction to cover residual differences between observed and simulated data. It is estimated to be, on average, 1% of the correction itself for muons from $Z \rightarrow \mu^+ \mu^-$ decays.

Corrections are also applied to the reconstructed muon momentum in simulation in order to precisely match the data. These corrections to the simulated momentum resolution and momentum scale are parameterised as an expansion in powers of the muon p_T , with each coefficient measured as a function of η and ϕ . The corrections are extracted from large data samples of $J/\psi \rightarrow \mu^+ \mu^-$ and $Z \rightarrow \mu^+ \mu^-$ decays, using techniques that reduce any residual biases and by directly calibrating the global re-fitted track [49]. Compared to the previously used corrections, this reduces the associated uncertainties by approximately a factor of four.

The momentum-scale corrections range from 0.1% to 0.3% for muons with p_T between 5 and 100 GeV. These account for inaccuracies in the estimation of the energy loss in the traversed material, local magnetic field inaccuracies, and geometrical distortions. The corrections to the momentum resolution for muons with p_T of 5–100 GeV are at the percent level. The main sources of systematic uncertainty for these corrections are the residual biases in the calibration method and the consistency of calibrations using $J/\psi \rightarrow \mu^+\mu^-$ or $Z \rightarrow \mu^+\mu^-$ decays separately. For muons from $Z \rightarrow \mu^+\mu^-$ decays, which have an average p_T of approximately 45 GeV, the momentum scale is determined with a precision better than 0.01%. The resolution is known with a precision of 0.4% for muons with $|\eta| < 1$, while for muons in high- $|\eta|$ regions the precision is approximately 1%.

A reconstructed electron consists of a cluster of energy deposits in the calorimeter and a matched ID track [50]. Variable-size clusters are created dynamically from calorimeter-energy deposits, improving the invariant-mass resolution of the four-lepton system, especially when bremsstrahlung photons are present. Electron ID tracks are fitted using an optimised Gaussian-sum filter (GSF) [51] that accounts for non-linear effects arising from energy loss through bremsstrahlung. Quality criteria are used to improve the purity of selected electron candidates. The quality of an electron candidate is evaluated by using a likelihood method that employs measurements from the tracking system and the calorimeter system, and quantities that combine both tracking and calorimeter information [51]. The ‘loose’ likelihood criteria, together with track hit requirements, are applied to electron candidates. Electrons are required to be isolated using both the calorimeter-based and track-based isolation variables as discussed in Ref. [13].

The energy of electrons is estimated from the calorimeter energy clusters, using a combination of simulation-based and data-driven corrections [50, 52]. A single simulation-based correction, which accounts for the energy lost in the material upstream of the calorimeter, the energy deposited in the cells neighbouring the cluster in η and ϕ , and the energy lost beyond the LAr calorimeter, is derived using multivariate regression algorithms. Data-driven corrections account for effects such as those associated with the material in front of the EM calorimeter and material between the presampler and the calorimeter, and the inter-calibration of the different calorimeter layers. The remaining energy-scale difference between data and simulation is parameterised by energy-independent linear corrections, defined in different regions of η . Similarly, deviations of the energy resolution in the simulation from that in the data are parameterised as an η -dependent additional term.

The main sources of systematic uncertainties in the electron-energy scale include uncertainties in the method used to extract the energy scale correction, as well as uncertainties due to the extrapolation of the energy scale from $Z \rightarrow e^+e^-$ events to electrons with different energies. A detailed explanation of these uncertainties can be found in Ref. [50]. In the case of electrons with E_T around 40 GeV, the total relative uncertainties range between 0.04% and 0.2% for most of the detector acceptance. For electrons with E_T around 10 GeV the relative uncertainty ranges between 0.3% and 0.8%.

Systematic uncertainties in the calorimeter-energy resolution for electrons arise from uncertainties in the modelling of the sampling term and in the measurement of the constant term in Z -boson decays, in the amount of material in front of the calorimeter, and in the modelling of the contribution to the resolution due to fluctuations in the pile-up from additional pp interactions in the same or neighbouring bunch crossings. The uncertainty in the energy resolution for electrons with transverse energy between 30 and 60 GeV varies between 5% and 10%.

5 Event selection

Events are required to contain at least four isolated leptons ($\ell = e, \mu$) emerging from a common vertex and forming two pairs of oppositely charged same-flavour leptons. Electrons are required to be within the geometrical acceptance of the inner detector ($|\eta| < 2.47$) and to have $E_T > 7$ GeV, while muons must be within the geometrical acceptance of the muon spectrometer ($|\eta| < 2.7$) and have $p_T > 5$ GeV (except for calorimeter-tagged muons, as explained in Section 4). At most one calorimeter-tagged or stand-alone muon is allowed per Higgs boson candidate. The three higher- $(p_T$ or E_T) leptons in each quadruplet are required to pass thresholds of 20, 15, and 10 GeV, respectively, and have $\Delta R(\ell, \ell') > 0.1$. Contributions from misidentified leptons are reduced by requiring the lepton tracks to have low transverse-impact-parameter significances and to be compatible with originating from a common vertex. A detailed description of the event selection can be found in Ref. [13].

The lepton pair with an invariant mass closest to the Z -boson mass in each quadruplet is referred to as the leading dilepton, while the remaining pair is referred to as the subleading dilepton. The selected quadruplets are separated into four subchannels, according to the flavour of the leading and subleading pairs. In order of decreasing expected selection efficiency and resolution, they are 4μ , $2e2\mu$, $2\mu2e$, and $4e$. The $m_{4\ell}$ resolution is about 1.5 GeV for subchannels with a subleading muon pair (4μ and $2e2\mu$) and about 2.1 GeV for subchannels with a subleading electron pair ($2\mu2e$ and $4e$). Only one quadruplet is selected from each event, based on the mass of the leading dilepton, the final state, and, for events with additional leptons, the value of the LO matrix element, as described in Ref. [13].

Final-state radiation (FSR) photons are searched for in all events following the procedure described in Ref. [13]. FSR candidates are defined as collinear if their angular separation from the nearest lepton of the quadruplet satisfies $\Delta R < 0.15$, and non-collinear otherwise. Collinear FSR candidates are considered only for muons from the leading dilepton, while non-collinear FSR candidates are considered for both muons and electrons from either the leading or the subleading dilepton. Only one FSR candidate is included in the quadruplet, with preference given to collinear FSR and to the candidate with the highest p_T . FSR photons are found in 4% of the events and their energy is included in the mass computation, improving the $m_{4\ell}$ resolution by about 1%.

Finally, the four-momenta of leptons in the leading pair are recomputed by performing a kinematic fit which constrains their invariant mass to the Z -boson mass, as discussed in Ref. [53]. The fit, which takes into account lepton and FSR kinematic information, their associated experimental uncertainties, and the Z -boson width, improves the $m_{4\ell}$ resolution by about 17% [9]. In the case of muons, the four-momenta reconstruction uncertainties were derived from simulation and are corrected to match those observed in data, using a large sample of $Z \rightarrow \mu^+\mu^-$ decays.

In the mass range $115 < m_{4\ell} < 130$ GeV, 313 candidate events are observed. The yield is in agreement with the expectation of 321 ± 14 events, 65% of which are predicted to be from the signal, assuming $m_H = 125$ GeV. The $m_{4\ell}$ distributions are shown in Figure 1 for each final state and in Figure 2 for the inclusive final state for the mass range of 105–160 GeV, which is used to determine the Higgs boson mass.

The dominant contribution to the background is non-resonant ZZ^* production, accounting for approximately 89% of the total background yield. The reducible background contributes approximately 9%. The VVV and tXX events are estimated to constitute approximately 2% of the total background. The residual combinatorial background, originating from events with additional prompt leptons, is found to be negligible [13].

5.1 Signal–background discriminant

To provide additional separation between the $H \rightarrow ZZ^* \rightarrow 4\ell$ signal and the $ZZ^* \rightarrow 4\ell$ background, a deep feed-forward neural network (NN) is employed. The NN is trained with Keras [54] using the TensorFlow [55] backend, following the method described in Ref. [13]. Signal events for training are taken from simulated samples with different masses of the Higgs boson, as described in Section 3, thus reducing the dependence of the discriminant on m_H .

The p_T and η of the four-lepton system are used as inputs to the NN, together with a matrix-element-based kinematic discriminant D_{ZZ^*} [53]. The discriminant D_{ZZ^*} is defined as $\ln(|\mathcal{M}_{HZZ^*}|^2/|\mathcal{M}_{ZZ^*}|^2)$ where \mathcal{M}_{HZZ^*} denotes the matrix element for leading-order (LO) $H \rightarrow ZZ^* \rightarrow 4\ell$ production and \mathcal{M}_{ZZ^*} the sum of the corresponding matrix elements for the $q\bar{q} \rightarrow ZZ^*$ and $gg \rightarrow ZZ^*$ continuum backgrounds, all calculated at LO with the `MADGRAPH 2.2.1` generator [33].

The distribution of the output of the NN, D_{NN} , is shown in Figure 3. The D_{NN} for each event is included in the final fit as an additional observable, as explained in Section 6. The additional separation between signal and background provided by the NN improves the precision of this measurement by 2%.

5.2 Event-level $m_{4\ell}$ resolution

The event-level $m_{4\ell}$ resolution, σ_i , is estimated using a quantile regression neural network (QRNN) [56]. The QRNN is trained on signal MC events using the Tensorflow library and the Keras Python application programming interface. The inputs are the p_T , η , and ϕ of the individual leptons, as well as the constrained four-lepton momentum and its uncertainty. The output of the QRNN for each final state is the predicted quantile of the difference between the reconstructed mass and the true mass of the four-lepton system. The targeted quantile is calibrated using a step-wise scanning procedure so that it results in an estimate that produces 68% confidence-level intervals when tested on simulated events.

The σ_i distributions are shown in Figure 4. Each event is assigned the σ_i estimated by the QRNN and employed in the likelihood fit to m_H . Taking into account the per-event resolution reduces the total expected uncertainty in m_H by 1%.

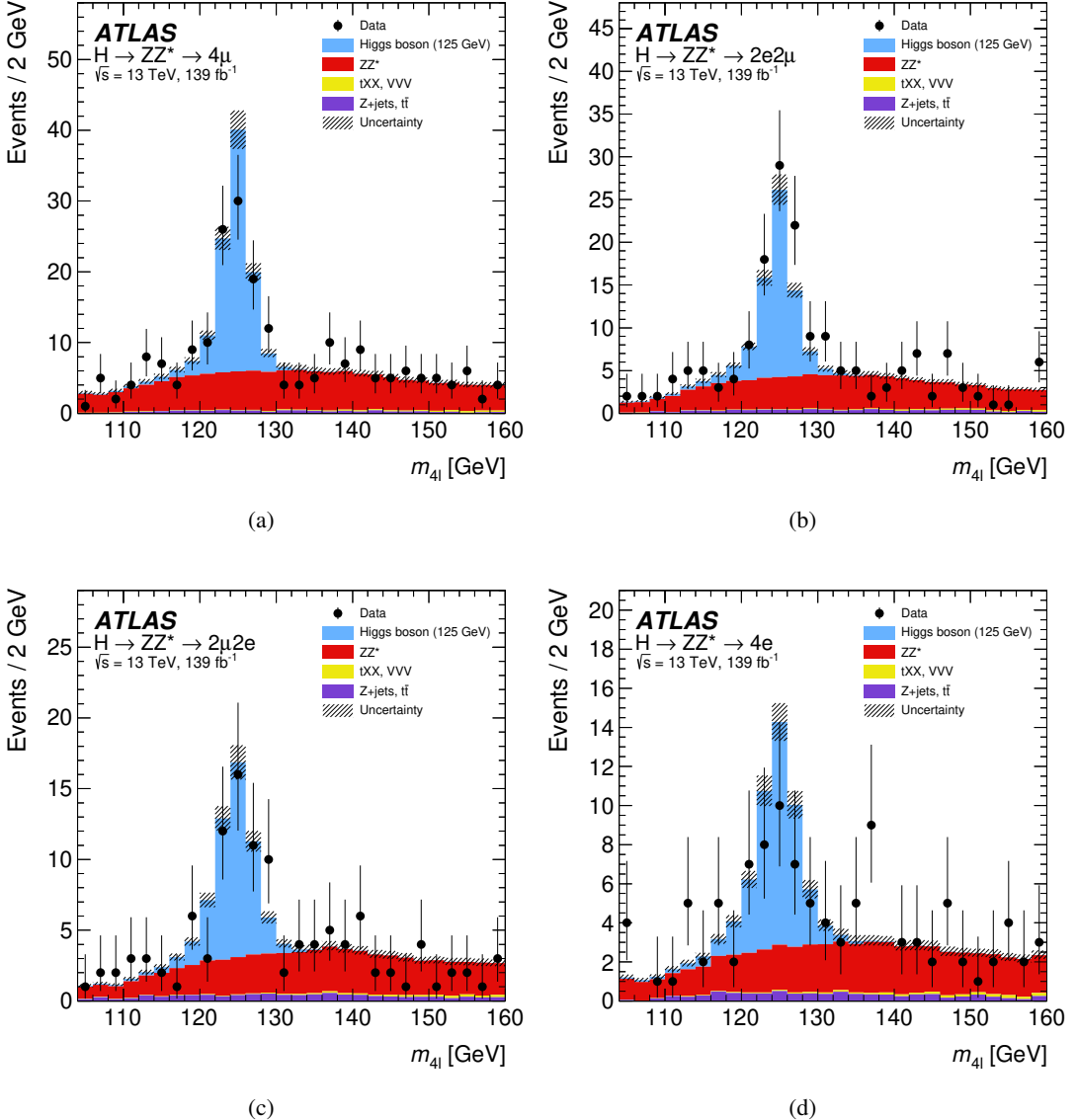


Figure 1: The observed and expected (pre-fit) m_{4l} distributions for the selected Higgs boson candidates, for the different decay final states (a) 4μ , (b) $2e2\mu$, (c) $2\mu 2e$, and (d) $4e$ events. The predicted number of events for these distributions is taken from simulation for the signal, ZZ^* , tXX , and VVV processes, while it is taken from the data-driven estimate (see Section 6) for the Z -jets and $t\bar{t}$ backgrounds. The total uncertainty in the prediction is shown by the hatched band, which also includes the theoretical uncertainties of the SM cross-section for the signal and the ZZ^* background. Higgs boson events in this plot are simulated with $m_H = 125$ GeV.

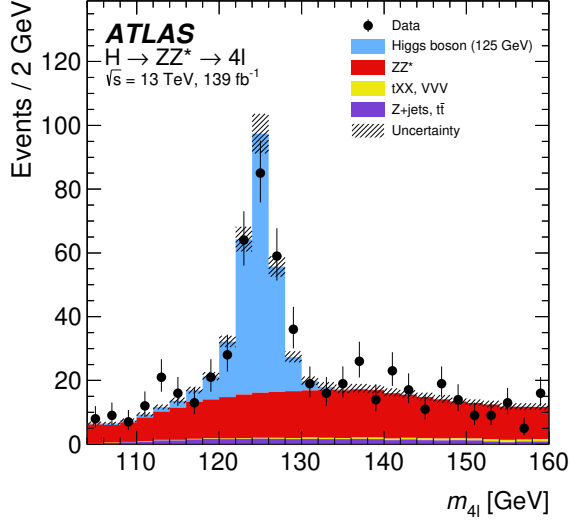


Figure 2: The observed and expected (pre-fit) m_{4l} distributions for the selected Higgs boson candidates. The predicted number of events for these distributions is taken from simulation for the signal, ZZ^* , tXX , and VVV processes, while it is taken from the data-driven estimate (see Section 6) for the Z -jets and $t\bar{t}$ backgrounds. The total uncertainty in the prediction is shown by the hatched band, which also includes the theoretical uncertainties of the SM cross-section for the signal and the ZZ^* background. Higgs boson events in this plot are simulated with $m_H = 125$ GeV.

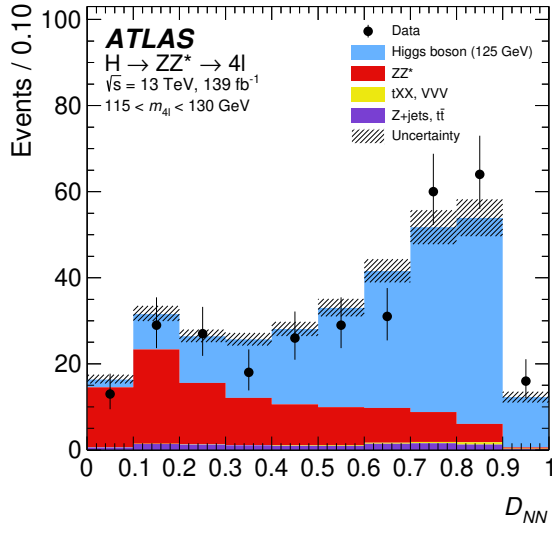


Figure 3: The observed and expected (pre-fit) D_{NN} distributions for the selected Higgs boson candidates. The predicted number of events for these distributions is taken from simulation for the signal, ZZ^* , tXX , and VVV processes, while it is taken from the data-driven estimate (see Section 6) for the Z -jets and $t\bar{t}$ backgrounds. The total uncertainty in the prediction is shown by the hatched band, which also includes the theoretical uncertainties of the SM cross-section for the signal and the ZZ^* background. Higgs boson events in this plot are simulated with $m_H = 125$ GeV.

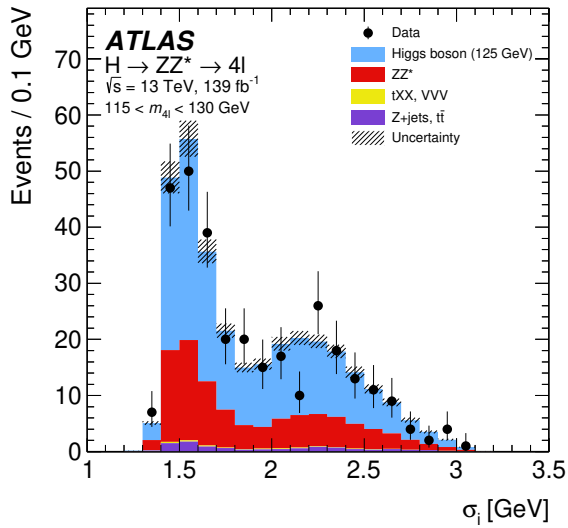


Figure 4: The observed and expected (pre-fit) event-level resolution σ_i distributions predicted by the QRNN for the selected Higgs boson candidates. The predicted number of events for these distributions is taken from simulation for the signal, ZZ^* , tXX , and VVV processes, while it is taken from the data-driven estimate (see Section 6) for the $Z+jets$ and $t\bar{t}$ backgrounds. The total uncertainty in the prediction is shown by the hatched band, which also includes the theoretical uncertainties of the SM cross-section for the signal and the ZZ^* background. Higgs boson events in this plot are simulated with $m_H = 125$ GeV. The 4μ and $2\mu 2e$ events typically have $\sigma_i \sim 1.5$ GeV, while the $2e 2\mu$ and $4e$ events typically have $\sigma_i \sim 2.1$ GeV.

6 Signal and background model

The Higgs boson $m_{4\ell}$ distribution is the result of the convolution of its theoretical line-shape, a narrow relativistic Breit–Wigner (BW) distribution of 4.1 MeV width [7] centred on m_H , with the detector response for the four-lepton invariant-mass distribution. The BW width is more than two orders of magnitude smaller than the $m_{4\ell}$ detector resolution. Therefore, the signal line-shape in $m_{4\ell}$ is completely dominated by the detector response.

The signal probability density function is modelled as

$$\begin{aligned}\mathcal{P}(m_{4\ell}, D_{NN}, \sigma_i | m_H) &= \mathcal{P}(m_{4\ell} | D_{NN}, \sigma_i, m_H) \cdot \mathcal{P}(D_{NN} | \sigma_i, m_H) \cdot \mathcal{P}(\sigma_i | m_H) \\ &\simeq \mathcal{P}(m_{4\ell} | D_{NN}, \sigma_i, m_H) \cdot \mathcal{P}(D_{NN} | m_H),\end{aligned}$$

where the following approximations are used:

- $\mathcal{P}(D_{NN} | \sigma_i, m_H) \simeq \mathcal{P}(D_{NN} | m_H)$ because the neural network discriminant does not directly depend on the per-event $m_{4\ell}$ resolution,
- $\mathcal{P}(\sigma_i | m_H) \simeq \mathcal{P}(\sigma_i)$ since the averaged per-event resolution does not depend on m_H within the range of 105 to 160 GeV used in this measurement, and
- $\mathcal{P}(\sigma_i)$ is omitted from the probability density function because it was observed that it has approximately the same distribution for signal and background events in the Higgs boson peak region. Dedicated checks of the assumption that $\mathcal{P}(\sigma_i)$ can be omitted have shown that this has negligible impact on the measurement.

The probability density function $\mathcal{P}(m_{4\ell} | D_{NN}, \sigma_i, m_H)$ in each subchannel is described by a double-sided Crystal Ball [57] probability density function that consists of a Gaussian core and two power-law tails.

The mean of the Gaussian core is parameterised as a function of m_H and D_{NN} for each subchannel λ as

$$a^\lambda \cdot (m_H - 125 \text{ GeV}) + b^\lambda(D_{NN}),$$

in order to decorrelate the uncertainties of the shifts in the mean reconstructed $m_{4\ell}$ due to the subchannel dependence from those due to the D_{NN} dependence. The a^λ parameters are consistent with unity within a few percent for all final states. The dependence of b^λ on D_{NN} is parameterised as a continuous function, and its values lie in the 124–125 GeV range for the $2\mu 2e$ and $4e$ final states, and between 124.6 GeV and 125 GeV for the $2e 2\mu$ and 4μ final states. The residual correlations between the m_H dependence of the mean and shape of the reconstructed $m_{4\ell}$ distribution, and the D_{NN} dependence of the mean have been checked with simulation and found to be negligible. The a^λ parameters and the b^λ functions are extracted from an unbinned maximum-likelihood fit to the combined ggF, VBF and VH samples, which were simulated with different values of m_H , as described in Section 3.

The standard deviation of the Gaussian core is expressed as a function of the predicted event-level resolution σ_i and is parameterised as a function of D_{NN} to account for a residual correlation between D_{NN} and σ_i . The parameters of the left tail of the double-sided Crystal Ball are parameterised as a function of D_{NN} only, while those of the right tail are found to be constant for a given final state.

The parameters of the signal model for each subchannel are derived by a simultaneous maximum-likelihood fit to signal MC samples for m_H values ranging from 123 GeV to 127 GeV. The resulting probability density function is shown in Figure 5 for the $m_H = 125$ GeV signal sample. The residual bias in the

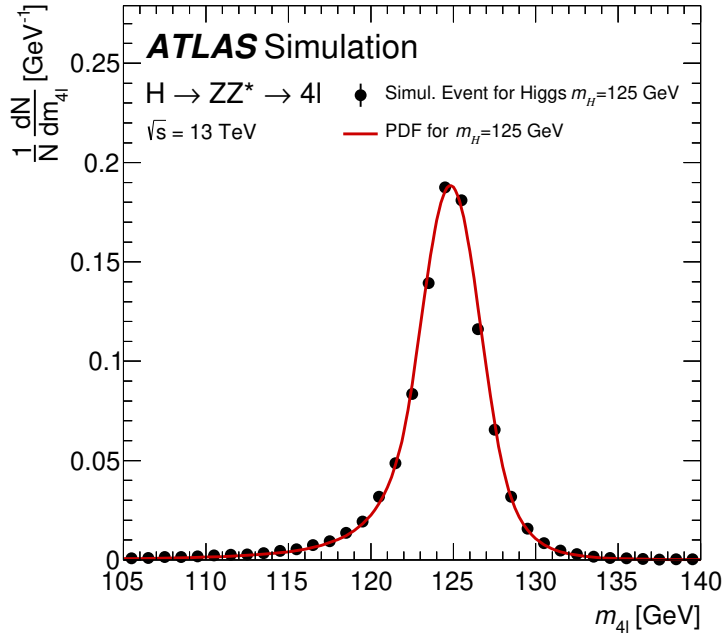


Figure 5: The probability density function derived from signal MC simulation using the per-event resolution (red line) is shown in comparison with the $m_{4\ell}$ distribution in signal MC simulation (black points) for $m_H = 125$ GeV. The probability density function is derived for each channel separately and they are added together assuming predicted yields. Both the probability density function and the MC simulation are normalised to unity.

measured m_H for the derived model, estimated by pseudo-experiments sampling MC events, is at the level of 6 MeV and is treated as an additional systematic uncertainty. In the fit of the model to the data, m_H can vary freely while the other parameters are constrained to vary in accordance with the impact of the relevant systematic uncertainties. Negligible biases in m_H are observed when fitting the model to simulated Higgs signal samples with different values of m_H .

The probability density functions for the ZZ^* and $tXX + VVV$ backgrounds are estimated as a function of $m_{4\ell}$ and D_{NN} for each subchannel from MC simulation. The background contributions from misidentified and non-isolated leptons are estimated from a data-control region [13], with only the dependence on $m_{4\ell}$ and D_{NN} parameterised using simulated samples.

The probability density functions for the backgrounds are smoothed using an adaptive kernel estimation technique, employing Gaussian kernels [58] to reduce statistical fluctuations. The effects of uncertainties that modify the shapes of probability density functions are described by using non-linear moment morphing [59] to interpolate between the nominal probability density functions and those accounting for the relevant systematic variations. Such uncertainties include the theoretical and experimental uncertainties for the ZZ^* and $tXX + VVV$ probability density functions and imperfect knowledge of the relative background composition for the reducible background's probability density function.

The $m_{4\ell}$ distribution is described by the sum of a signal distribution and the distributions of the backgrounds. The normalisations of the signal contribution and the ZZ^* process in each subchannel are free parameters and extracted directly from the fit to data, while those of the reducible background in each channel are constrained according to estimates obtained from data, using minimal input from simulation and following

the methodology described in Ref. [13]. The normalisation of the $tXX + VVV$ background is constrained according to the uncertainties in the theory prediction.

The fit model was validated by utilising a two-step unblinding process, where the same, unknown, bias is applied to all events in the observed dataset and the likelihood model, as described in Section 7, is fitted to it. No significant changes to the compatibility between channels or to any free or constrained parameters, with the exception of m_H , are observed when this bias is removed.

7 Results

The mass measurement is performed by maximising the profile-likelihood ratio [60, 61]

$$\lambda(m_H) = \frac{\mathcal{L}(m_H, \hat{\theta}(m_H))}{\mathcal{L}(\hat{m}_H, \hat{\theta})},$$

where \hat{m}_H and $\hat{\theta}$ denote the unconditional maximum-likelihood estimates of the parameters of the likelihood function \mathcal{L} , while $\hat{\theta}$ is the conditional maximum-likelihood estimate of the parameters θ for a fixed value of the parameter of interest, m_H . Systematic uncertainties and their correlations are modelled by introducing nuisance parameters θ with priors described by Gaussian or log-normal functions that reflect the uncertainties in the values of the nuisance parameters.

The estimate of m_H is extracted by performing a simultaneous unbinned maximum-likelihood fit to the four subchannels (4μ , $2e2\mu$, $2\mu2e$, and $4e$) in the $m_{4\ell}$ range between 105 and 160 GeV. The expected and observed yields, along with the signal-to-background ratio, are shown in Table 1 for the signal region defined by limiting the data to $m_{4\ell}$ between 115 and 130 GeV.

The free parameters of the fit are m_H , the signal normalisation, and background normalisations for each of the four subchannels, while the nuisance parameters associated with the systematic uncertainties are constrained by their respective priors. Figure 6 shows the $m_{4\ell}$ distribution of the data together with the result of the fit to the $H \rightarrow ZZ^* \rightarrow 4\ell$ candidates. The small shape fluctuations in the background prediction arise from the integrations of the background probability density functions; their effects on the mass fit are negligible. The fit results in

$$m_H = 124.99 \pm 0.18(\text{stat.}) \pm 0.04(\text{syst.}) \text{ GeV}.$$

All fitted normalisations are found to be compatible with the SM expectations. The fit for m_H is also performed independently for each decay channel. The $m_{4\ell}$ distributions for the four channels are shown in Figure 7. The resulting profile-likelihood-ratio variation as a function of m_H and the resulting fitted values are compared with those of the combined fit in Figure 8. The m_H measurements from the individual channels are compatible with the combined measurement, with a p -value of 0.82.

The statistical uncertainty of m_H is estimated by fixing all nuisance parameters associated with systematic uncertainties to their best-fit values, leaving all remaining parameters unconstrained. The total systematic uncertainty is estimated by subtracting the square of the statistical uncertainty from the square of the total uncertainty and calculating the square root. Table 2 shows the leading contributions to the systematic uncertainty of m_H . The uncertainties in the electron energy scale and in the muon momentum scale, resolution, and sagitta bias correction are described in Section 4. Other sources, including background modelling and simulation statistics, contribute less than 5 MeV. The total uncertainty is in agreement

Table 1: The observed and expected (pre-fit) yields for the different decay final states in the region with $m_{4\ell}$ between 115 and 130 GeV. The predicted number of events is taken from simulation for the signal, ZZ^* , tXX , and VVV processes, while for $Z+jets$ and $t\bar{t}$ it is taken from the data-driven estimate (see Section 6). The uncertainty in the prediction includes the theoretical uncertainties of the SM cross-section for the signal and the ZZ^* background. Higgs boson yields are determined using simulation with $m_H = 125$ GeV.

Final state	Higgs	ZZ , tXX , VVV	Reducible backgrounds	Expected total yield	Observed yield	S/B
4μ	78 ± 5	38.7 ± 2.2	2.84 ± 0.17	120 ± 5	115	1.89
$2e2\mu$	53.4 ± 3.2	26.7 ± 1.4	3.02 ± 0.19	83.1 ± 3.5	94	1.80
$2\mu2e$	41.2 ± 3.0	17.9 ± 1.3	3.4 ± 0.5	62.5 ± 3.3	59	1.93
$4e$	36.2 ± 2.7	15.7 ± 1.6	2.83 ± 0.35	54.8 ± 3.2	45	1.95
Total	209 ± 13	99 ± 6	12.2 ± 0.9	321 ± 14	313	1.88

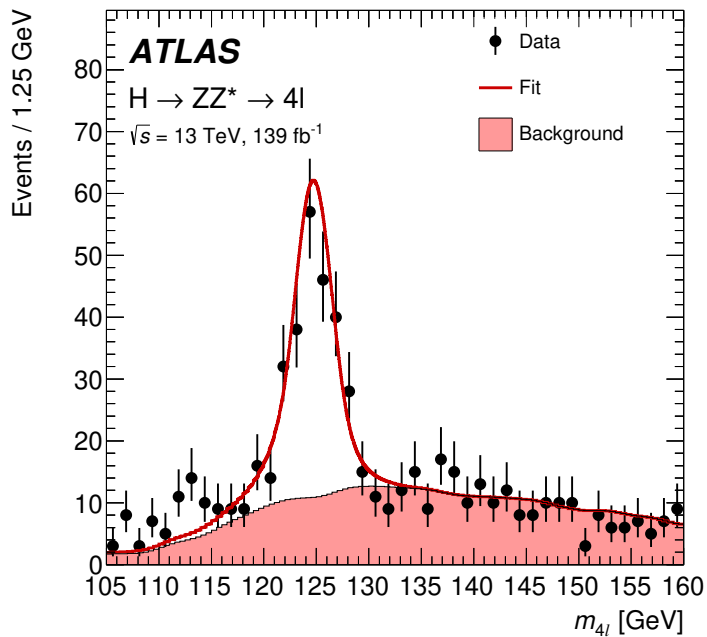


Figure 6: The $m_{4\ell}$ data distribution from all subchannels combined (black points) is shown along with the signal-plus-background post-fit probability density function (red line).

with the expectation of 0.19 GeV and is dominated by the statistical component. Figure 9 shows the distribution of the expected uncertainty in m_H obtained by fitting a set of pseudo-experiments assuming $m_H = 125$ GeV.

The result of this measurement is combined with the measurement of m_H using the Run 1 dataset in the same final states, which was $m_H = 124.51 \pm 0.52$ [9]. The correlation scheme for the systematic uncertainties of the two measurements follows the one used in Ref. [11], where only the uncertainties in the lepton calibration were considered correlated. In this combination, the electron calibration uncertainty is correlated between the two measurements, while the muon calibration systematic uncertainty is uncorrelated

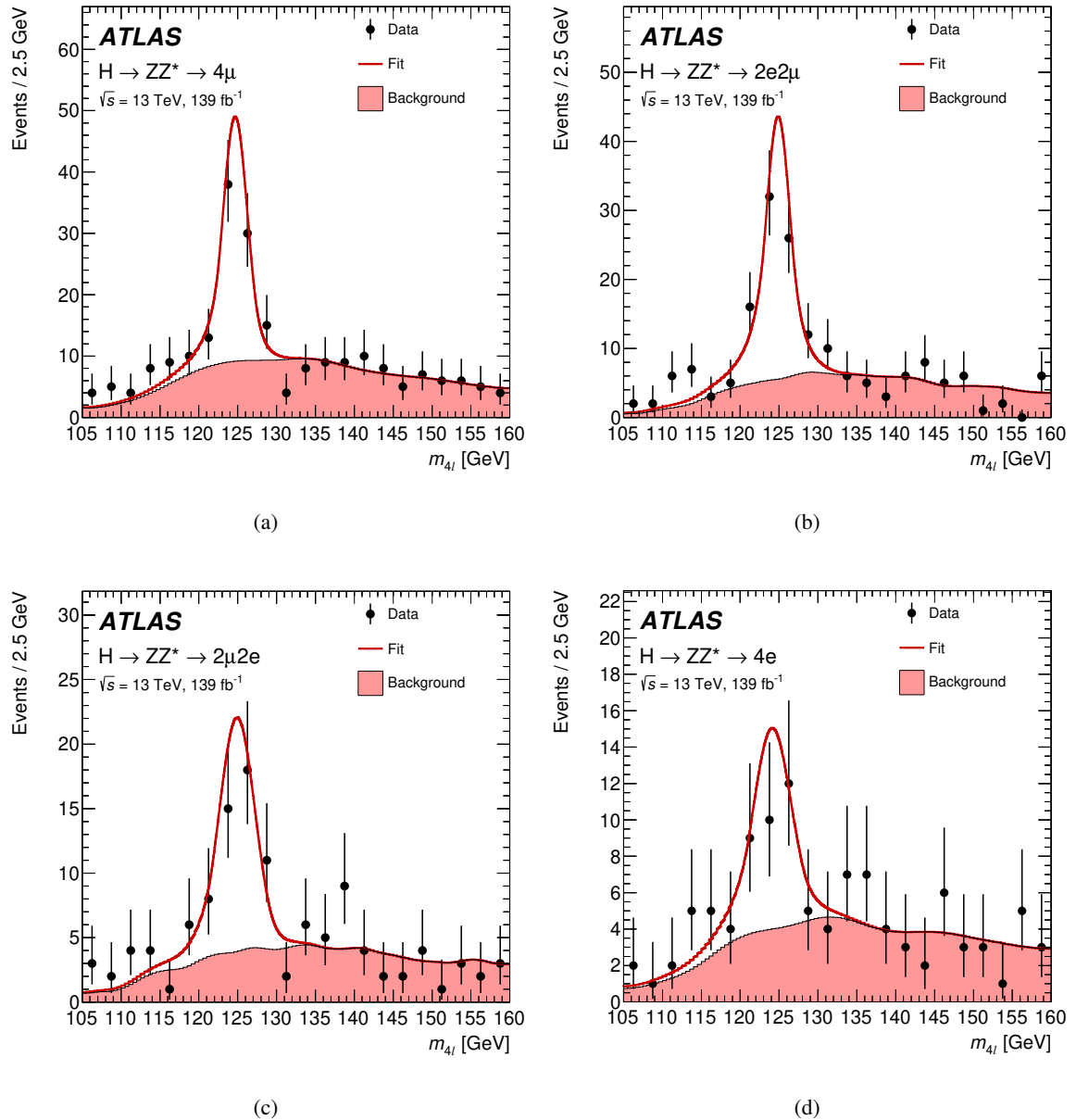


Figure 7: The $m_{4\ell}$ data distribution (black points) for (a) 4μ , (b) $2e2\mu$, (c) $2\mu2e$, and (d) $4e$ events is shown along with the signal-plus-background post-fit probability density function (red line).

Table 2: Largest contributions to the systematic uncertainty of m_H .

Systematic Uncertainty	Contribution [MeV]
Muon momentum scale	± 28
Electron energy scale	± 19
Signal-process theory	± 14

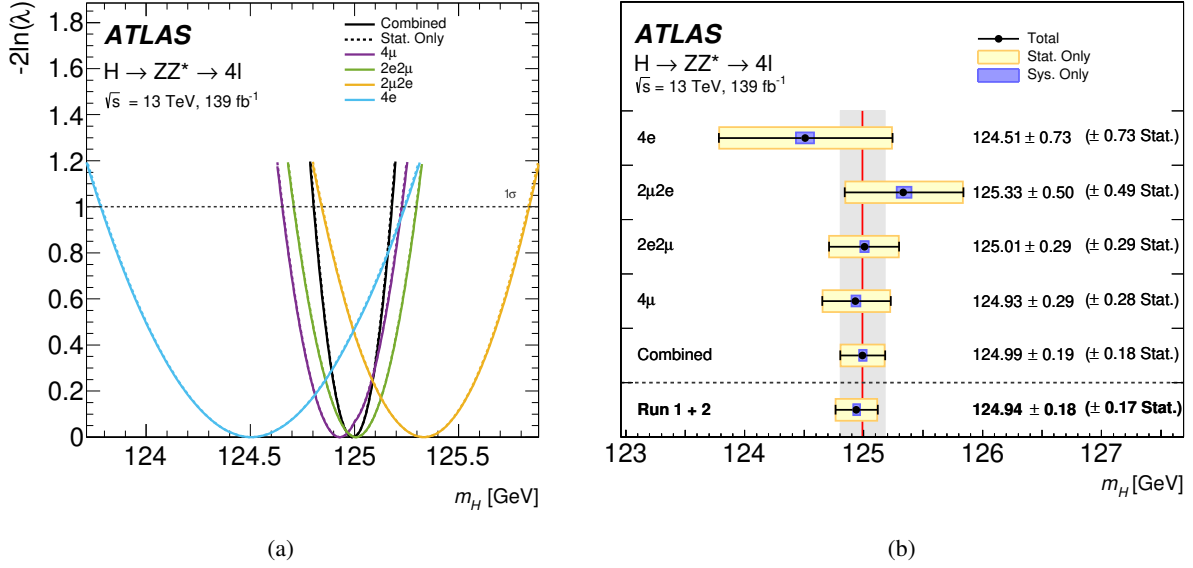


Figure 8: The test statistic, $-2\ln(\lambda)$, values as a function of m_H are shown in (a) for the fit in each of the final states 4μ (purple), $2e2\mu$ (green), $2\mu2e$ (orange), and $4e$ (blue), and for the combined fit (black), both with (solid lines) and without (dashed lines) systematic uncertainties. The horizontal dashed line indicates the location of the one- σ uncertainty. The fit results obtained in each final state are shown in (b) together with the combined result. The uncertainty bar on each point is the total statistical and systematic uncertainty; the brackets show the statistical uncertainty only. The vertical (red) line indicates the combined Run 2 result, and the grey band its total uncertainty.

due to the use of improved and independent techniques, as described in Section 4. Systematic uncertainties are reduced by about 14% when using this correlation scheme. The combined result, calculated by combining the likelihoods of the two measurements is

$$m_H = 124.94 \pm 0.17(\text{stat.}) \pm 0.03(\text{syst.}) \text{ GeV},$$

which has slightly smaller statistical and systematic uncertainties. The p -value for the two individual results, assuming the Higgs boson mass is the combined value, is 0.4.

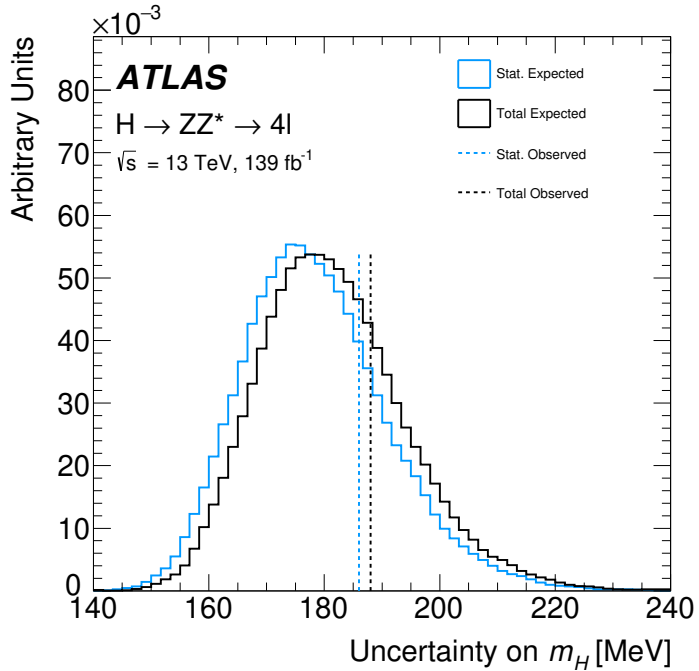


Figure 9: The distributions of the total m_H uncertainty from pseudo-experiments assuming $m_H = 125$ GeV are shown, for when the fit does (black) and does not (blue) take into account systematic uncertainties. The solid lines correspond to the expected uncertainty distribution from pseudo-experiments, while the vertical dashed lines indicate the observed values of the uncertainties. The one-sided p -value for compatibility between the observed and expected total uncertainties is 0.28.

8 Summary

The mass of the Higgs boson is measured from a maximum-likelihood fit to the invariant mass and the predicted invariant-mass resolution of the $H \rightarrow ZZ^* \rightarrow 4\ell$ decay channel. The results are obtained from the full Run 2 pp collision data sample recorded by the ATLAS experiment at the CERN Large Hadron Collider at a centre-of-mass energy of 13 TeV, corresponding to an integrated luminosity of 139 fb^{-1} . The measurement is based on the latest calibrations of muons and electrons, and on improvements to the analysis techniques used to obtain the previous result using data collected by ATLAS in 2015 and 2016.

The measured value of the Higgs boson mass for the $H \rightarrow ZZ^* \rightarrow 4\ell$ channel is

$$m_H = 124.99 \pm 0.18(\text{stat.}) \pm 0.04(\text{syst.}) \text{ GeV.}$$

Thanks to a larger dataset, improved experimental techniques, and more precise lepton calibration, the statistical uncertainty of the measurement has been reduced by a factor of two and the systematic uncertainty by about 20% relative to the previous Run 2 published result.

This measurement is combined with the previous one obtained in the same channel with ATLAS Run 1 data. The result of the combination is

$$m_H = 124.94 \pm 0.17(\text{stat.}) \pm 0.03(\text{syst.}) \text{ GeV.}$$

This is the most precise measurement of m_H in the $H \rightarrow ZZ^* \rightarrow 4\ell$ channel by the ATLAS Collaboration.

References

- [1] ATLAS Collaboration, *Observation of a new particle in the search for the Standard Model Higgs boson with the ATLAS detector at the LHC*, *Phys. Lett. B* **716** (2012) 1, arXiv: [1207.7214 \[hep-ex\]](https://arxiv.org/abs/1207.7214).
- [2] CMS Collaboration, *Observation of a new boson at a mass of 125 GeV with the CMS experiment at the LHC*, *Phys. Lett. B* **716** (2012) 30, arXiv: [1207.7235 \[hep-ex\]](https://arxiv.org/abs/1207.7235).
- [3] F. Englert and R. Brout, *Broken symmetry and the mass of gauge vector mesons*, *Phys. Rev. Lett.* **13** (1964) 321.
- [4] P. W. Higgs, *Broken symmetries and the masses of gauge bosons*, *Phys. Rev. Lett.* **13** (1964) 508.
- [5] G. Guralnik, C. Hagen and T. Kibble, *Global conservation laws and massless particles*, *Phys. Rev. Lett.* **13** (1964) 585.
- [6] M. Sher, *Electroweak Higgs potential and vacuum stability*, *Physics Reports* **179** (1989) 273, ISSN: 0370-1573, URL: <https://www.sciencedirect.com/science/article/pii/0370157389900616>.
- [7] D. de Florian et al., *Handbook of LHC Higgs Cross Sections: 4. Deciphering the Nature of the Higgs Sector*, (2016), arXiv: [1610.07922 \[hep-ph\]](https://arxiv.org/abs/1610.07922).
- [8] ATLAS and CMS Collaborations, *Combined Measurement of the Higgs Boson Mass in pp Collisions at $\sqrt{s} = 7$ and 8 TeV with the ATLAS and CMS Experiments*, *Phys. Rev. Lett.* **114** (2015) 191803, arXiv: [1503.07589 \[hep-ex\]](https://arxiv.org/abs/1503.07589).
- [9] ATLAS Collaboration, *Measurement of the Higgs boson mass from the $H \rightarrow \gamma\gamma$ and $H \rightarrow ZZ^* \rightarrow 4\ell$ channels in pp collisions at center-of-mass energies of 7 and 8 TeV with the ATLAS detector*, *Phys. Rev. D* **90** (2014) 052004, arXiv: [1406.3827 \[hep-ex\]](https://arxiv.org/abs/1406.3827).
- [10] CMS Collaboration, *Precise determination of the mass of the Higgs boson and tests of compatibility of its couplings with the standard model predictions using proton collisions at 7 and 8 TeV*, *Eur. Phys. J. C* **75** (2015) 212, arXiv: [1412.8662 \[hep-ex\]](https://arxiv.org/abs/1412.8662).
- [11] ATLAS Collaboration, *Measurement of the Higgs boson mass in the $H \rightarrow ZZ^* \rightarrow 4\ell$ and $H \rightarrow \gamma\gamma$ channels with $\sqrt{s} = 13$ TeV pp collisions using the ATLAS detector*, *Phys. Lett. B* **784** (2018) 345, arXiv: [1806.00242 \[hep-ex\]](https://arxiv.org/abs/1806.00242).
- [12] CMS Collaboration, *A measurement of the Higgs boson mass in the diphoton decay channel*, *Phys. Lett. B* **805** (2020) 135425, arXiv: [2002.06398 \[hep-ex\]](https://arxiv.org/abs/2002.06398).
- [13] ATLAS Collaboration, *Higgs boson production cross-section measurements and their EFT interpretation in the 4ℓ decay channel at $\sqrt{s} = 13$ TeV with the ATLAS detector*, *Eur. Phys. J. C* **80** (2020) 957, arXiv: [2004.03447 \[hep-ex\]](https://arxiv.org/abs/2004.03447), Erratum: *Eur. Phys. J. C* **81** (2021) 29.
- [14] ATLAS Collaboration, *The ATLAS Experiment at the CERN Large Hadron Collider*, *JINST* **3** (2008) S08003.

[15] ATLAS Collaboration, *ATLAS Insertable B-Layer Technical Design Report*, ATLAS-TDR-19; CERN-LHCC-2010-013, 2010, URL: <https://cds.cern.ch/record/1291633>, Addendum: ATLAS-TDR-19-ADD-1; CERN-LHCC-2012-009, 2012, URL: <https://cds.cern.ch/record/1451888>.

[16] B. Abbott et al., *Production and integration of the ATLAS Insertable B-Layer*, *JINST* **13** (2018) T05008, arXiv: [1803.00844 \[physics.ins-det\]](https://arxiv.org/abs/1803.00844).

[17] ATLAS Collaboration, *Performance of the ATLAS trigger system in 2015*, *Eur. Phys. J. C* **77** (2017) 317, arXiv: [1611.09661 \[hep-ex\]](https://arxiv.org/abs/1611.09661).

[18] ATLAS Collaboration, *The ATLAS Collaboration Software and Firmware*, ATL-SOFT-PUB-2021-001, 2021, URL: <https://cds.cern.ch/record/2767187>.

[19] ATLAS Collaboration, *Performance of the ATLAS muon triggers in Run 2*, *JINST* **15** (2020) P09015, arXiv: [2004.13447 \[hep-ex\]](https://arxiv.org/abs/2004.13447).

[20] ATLAS Collaboration, *Performance of electron and photon triggers in ATLAS during LHC Run 2*, *Eur. Phys. J. C* **80** (2020) 47, arXiv: [1909.00761 \[hep-ex\]](https://arxiv.org/abs/1909.00761).

[21] ATLAS Collaboration, *ATLAS data quality operations and performance for 2015–2018 data-taking*, *JINST* **15** (2020) P04003, arXiv: [1911.04632 \[physics.ins-det\]](https://arxiv.org/abs/1911.04632).

[22] ATLAS Collaboration, *Measurements of the Higgs boson inclusive and differential fiducial cross sections in the 4ℓ decay channel at $\sqrt{s} = 13$ TeV*, *Eur. Phys. J. C* **80** (2020) 942, arXiv: [2004.03969 \[hep-ex\]](https://arxiv.org/abs/2004.03969).

[23] K. Hamilton, P. Nason, E. Re and G. Zanderighi, *NNLOPS simulation of Higgs boson production*, *JHEP* **10** (2013) 222, arXiv: [1309.0017 \[hep-ph\]](https://arxiv.org/abs/1309.0017).

[24] K. Hamilton, P. Nason and G. Zanderighi, *Finite quark-mass effects in the NNLOPS POWHEG+MiNLO Higgs generator*, *JHEP* **05** (2015) 140, arXiv: [1501.04637 \[hep-ph\]](https://arxiv.org/abs/1501.04637).

[25] S. Alioli, P. Nason, C. Oleari and E. Re, *A general framework for implementing NLO calculations in shower Monte Carlo programs: the POWHEG BOX*, *JHEP* **06** (2010) 043, arXiv: [1002.2581 \[hep-ph\]](https://arxiv.org/abs/1002.2581).

[26] P. Nason, *A new method for combining NLO QCD with shower Monte Carlo algorithms*, *JHEP* **11** (2004) 040, arXiv: [hep-ph/0409146](https://arxiv.org/abs/hep-ph/0409146).

[27] S. Frixione, P. Nason and C. Oleari, *Matching NLO QCD computations with parton shower simulations: the POWHEG method*, *JHEP* **11** (2007) 070, arXiv: [0709.2092 \[hep-ph\]](https://arxiv.org/abs/0709.2092).

[28] K. Hamilton, P. Nason and G. Zanderighi, *MINLO: multi-scale improved NLO*, *JHEP* **10** (2012) 155, arXiv: [1206.3572 \[hep-ph\]](https://arxiv.org/abs/1206.3572).

[29] J. M. Campbell et al., *NLO Higgs boson production plus one and two jets using the POWHEG BOX, MadGraph4 and MCFM*, *JHEP* **07** (2012) 092, arXiv: [1202.5475 \[hep-ph\]](https://arxiv.org/abs/1202.5475).

[30] K. Hamilton, P. Nason, C. Oleari and G. Zanderighi, *Merging H/W/Z + 0 and 1 jet at NLO with no merging scale: a path to parton shower + NNLO matching*, *JHEP* **05** (2013) 082, arXiv: [1212.4504 \[hep-ph\]](https://arxiv.org/abs/1212.4504).

[31] S. Catani and M. Grazzini, *Next-to-Next-to-Leading-Order Subtraction Formalism in Hadron Collisions and its Application to Higgs-boson Production at the Large Hadron Collider*, *Phys. Rev. Lett.* **98** (2007) 222002, arXiv: [hep-ph/0703012 \[hep-ph\]](https://arxiv.org/abs/hep-ph/0703012).

[32] J. Butterworth et al., *PDF4LHC recommendations for LHC Run II*, *J. Phys. G* **43** (2016) 023001, arXiv: [1510.03865](https://arxiv.org/abs/1510.03865) [hep-ph].

[33] J. Alwall et al., *The automated computation of tree-level and next-to-leading order differential cross sections, and their matching to parton shower simulations*, *JHEP* **07** (2014) 079, arXiv: [1405.0301](https://arxiv.org/abs/1405.0301) [hep-ph].

[34] M. Wiesemann et al., *Higgs production in association with bottom quarks*, *JHEP* **02** (2015) 132, arXiv: [1409.5301](https://arxiv.org/abs/1409.5301) [hep-ph].

[35] R. D. Ball et al., *Parton distributions for the LHC run II*, *JHEP* **04** (2015) 040, arXiv: [1410.8849](https://arxiv.org/abs/1410.8849) [hep-ph].

[36] D. J. Lange, *The EvtGen particle decay simulation package*, *Nucl. Instrum. Meth. A* **462** (2001) 152.

[37] T. Sjöstrand, S. Mrenna and P. Skands, *A brief introduction to PYTHIA 8.1*, *Comput. Phys. Commun.* **178** (2008) 852, arXiv: [0710.3820](https://arxiv.org/abs/0710.3820) [hep-ph].

[38] T. Gleisberg et al., *Event generation with SHERPA 1.1*, *JHEP* **02** (2009) 007, arXiv: [0811.4622](https://arxiv.org/abs/0811.4622) [hep-ph].

[39] T. Gleisberg and S. Höche, *Comix, a new matrix element generator*, *JHEP* **12** (2008) 039, arXiv: [0808.3674](https://arxiv.org/abs/0808.3674) [hep-ph].

[40] F. Cascioli, P. Maierhöfer and S. Pozzorini, *Scattering Amplitudes with Open Loops*, *Phys. Rev. Lett.* **108** (2012) 111601, arXiv: [1111.5206](https://arxiv.org/abs/1111.5206) [hep-ph].

[41] E. Bothmann et al., *Event generation with Sherpa 2.2*, *SciPost Phys.* **7** (2019) 034, arXiv: [1905.09127](https://arxiv.org/abs/1905.09127) [hep-ph].

[42] ATLAS Collaboration, *The ATLAS Simulation Infrastructure*, *Eur. Phys. J. C* **70** (2010) 823, arXiv: [1005.4568](https://arxiv.org/abs/1005.4568) [physics.ins-det].

[43] GEANT4 Collaboration, S. Agostinelli et al., *GEANT4 – a simulation toolkit*, *Nucl. Instrum. Meth. A* **506** (2003) 250.

[44] ATLAS Collaboration, *The Pythia 8 A3 tune description of ATLAS minimum bias and inelastic measurements incorporating the Donnachie–Landshoff diffractive model*, ATL-PHYS-PUB-2016-017, 2016, URL: <https://cds.cern.ch/record/2206965>.

[45] R. D. Ball et al., *Parton distributions with LHC data*, *Nucl. Phys. B* **867** (2013) 244, arXiv: [1207.1303](https://arxiv.org/abs/1207.1303) [hep-ph].

[46] ATLAS Collaboration, *Muon reconstruction and identification efficiency in ATLAS using the full Run 2 pp collision data set at $\sqrt{s} = 13$ TeV*, *Eur. Phys. J. C* **81** (2021) 578, arXiv: [2012.00578](https://arxiv.org/abs/2012.00578) [hep-ex].

[47] ATLAS Collaboration, *Alignment of the ATLAS Inner Detector in Run-2*, *Eur. Phys. J. C* **80** (2020) 1194, arXiv: [2007.07624](https://arxiv.org/abs/2007.07624) [hep-ex].

[48] ATLAS Collaboration, *Performance of the muon spectrometer alignment in 2017 and 2018 data*, ATL-MUON-PUB-2021-002, 2021, URL: <https://cds.cern.ch/record/2753329>.

[49] ATLAS Collaboration, *Run II muon calibration*, in preparation, will be submitted in parallel to this paper (2022), URL: <https://atlas-glance.cern.ch/atlas/analysis/analyses/details?id=6958>.

[50] ATLAS Collaboration, *Electron and photon performance measurements with the ATLAS detector using the 2015–2017 LHC proton–proton collision data*, *JINST* **14** (2019) P12006, arXiv: [1908.00005 \[hep-ex\]](https://arxiv.org/abs/1908.00005).

[51] ATLAS Collaboration, *Electron reconstruction and identification in the ATLAS experiment using the 2015 and 2016 LHC proton–proton collision data at $\sqrt{s} = 13$ TeV*, *Eur. Phys. J. C* **79** (2019) 639, arXiv: [1902.04655 \[hep-ex\]](https://arxiv.org/abs/1902.04655).

[52] ATLAS Collaboration, *Electron and photon energy calibration with the ATLAS detector using 2015–2016 LHC proton–proton collision data*, *JINST* **14** (2019) P03017, arXiv: [1812.03848 \[hep-ex\]](https://arxiv.org/abs/1812.03848).

[53] ATLAS Collaboration, *Measurements of Higgs boson production and couplings in the four-lepton channel in pp collisions at center-of-mass energies of 7 and 8 TeV with the ATLAS detector*, *Phys. Rev. D* **91** (2015) 012006, arXiv: [1408.5191 \[hep-ex\]](https://arxiv.org/abs/1408.5191).

[54] F. Chollet et al., *Keras*, 2015, URL: <https://keras.io>.

[55] Martin Abadi et al., *TensorFlow: Large-Scale Machine Learning on Heterogeneous Systems*, Software available from tensorflow.org, 2015, URL: <https://www.tensorflow.org/>.

[56] H. White, ‘Nonparametric Estimation of Conditional Quantiles Using Neural Networks’, *Computing Science and Statistics*, New York, NY: Springer New York, 1992 190.

[57] ATLAS Collaboration, *Search for Scalar Diphoton Resonances in the Mass Range 65–600 GeV with the ATLAS Detector in pp Collision Data at $\sqrt{s} = 8$ TeV*, *Phys. Rev. Lett.* **113** (2014) 171801, arXiv: [1407.6583 \[hep-ex\]](https://arxiv.org/abs/1407.6583).

[58] K. Cranmer, *Kernel estimation in high-energy physics*, *Comput. Phys. Commun.* **136** (2001) 198, arXiv: [hep-ex/0011057 \[hep-ex\]](https://arxiv.org/abs/hep-ex/0011057).

[59] M. Baak, S. Gadatsch, R. Harrington and W. Verkerke, *Interpolation between multi-dimensional histograms using a new non-linear moment morphing method*, *Nucl. Instrum. Meth. A* **771** (2015) 39, ISSN: 0168-9002, URL: <http://dx.doi.org/10.1016/j.nima.2014.10.033>.

[60] ATLAS Collaboration, *Combined search for the Standard Model Higgs boson in pp collisions at $\sqrt{s} = 7$ TeV with the ATLAS detector*, *Phys. Rev. D* **86** (2012) 032003, arXiv: [1207.0319 \[hep-ex\]](https://arxiv.org/abs/1207.0319).

[61] G. Cowan, K. Cranmer, E. Gross and O. Vitells, *Asymptotic formulae for likelihood-based tests of new physics*, *Eur. Phys. J. C* **71** (2011) 1554, arXiv: [1007.1727 \[physics.data-an\]](https://arxiv.org/abs/1007.1727), Erratum: *Eur. Phys. J. C* **73** (2013) 2501.